Design of a porous material with isotropic negative Poisson's ratio

Giorgio Carta[a], Michele Brun[a,*], Antonio Baldi[a]

[a]*Dipartimento di Ingegneria Meccanica, Chimica e dei Materiali, Università di Cagliari, Piazza d'Armi, 09123 Cagliari, Italy*

Abstract

This paper proposes the design of a two-dimensional porous solid with omnidirectional negative Poisson's ratio. The hexagonal periodic distribution of the pores makes the effective behavior isotropic. Both experimental tests and numerical simulations have been performed to determine the effective properties of the porous solid. A parametric study on the effect of the geometrical microstructural parameters is also presented. This auxetic structure is easy to fabricate and can be very useful in several engineering applications.

Keywords:
Auxetic, negative Poisson's ratio, metamaterials, isotropy, porous medium, Digital Image Correlation, photoelasticity

1. Introduction

Most natural materials are characterized by a positive Poisson's ratio, namely they are observed to contract (expand) laterally when stretched (compressed) longitudinally. Nonetheless, the classical theory of elasticity does not preclude the existence of materials with negative Poisson's ratio, known also as 'auxetic' after Evans (1991). For linear isotropic materials constitutive stability imposes the condition that the Poisson's ratio lies in the interval $(-1, 0.5)$ (Timoshenko (1955)), while for anisotropic materials the Poisson's ratio is unbounded along specific directions and a stability domain can de-

*Corresponding author
Email addresses: giorgio_carta@unica.it (Giorgio Carta), mbrun@unica.it (Michele Brun), antonio.baldi@dimcm.unica.it (Antonio Baldi)

fined in a proper $n-$dimensional space, as shown by Norris (2006) for cubic materials.

Love (1944) was among the first to propose an example of an auxetic material and he showed that the Poisson's ratio of cubic crystals of pyrite is nearly equal to $-1/7$. Natural materials exhibiting a negative Poisson's ratio include silicates (Yeganeh-Haeri et al. (1992)), cubic elemental metals (Baugham et al. (1998)), zeolites (Grima et al. (2000, 2007)) and ceramics (Song et al. (2008)). Lakes (1987) presented the first designed auxetic material, consisting of a reentrant foam. Using topology optimisation Sigmund (1994) showed numerical results concerning materials with Poisson's ratio equal to -1, constructed from cells based on truss elements or continuous discs. Since these trailblazing works many artificially-made auxetic models have been proposed, based on different mechanisms such as reentrant units (Choi and Lakes (1995); Scarpa and Tomlin (2000)), chirality (Prall and Lakes (1997); Grima et al. (2008); Spadoni and Ruzzene (2012)), rigid rotating units (Grima et al. (2005); Grima and Gatt (2010)) and elastic instability (Bertoldi et al. (2010); Shen et al. (2014)). Recently, Grima and Gatt (2010) and Taylor et al. (2014) showed that metallic sheets with orthogonal voids, having two-dimensional cubic symmetry, are auxetic for specific values of the porosity and of the voids shape. Chen et al. (2013) carried out a numerical and experimental investigation on a fiber-reinforced composite flexible skin with in-plane negative Poisson's ratio. Chen et al. (2014) studied a curved cellular structure, manufactured by using Kirigami techniques, that is characterized by a null Poisson's ratio. Cabras and Brun (2014) analyzed and fabricated two-dimensional lattice structures, with isotropic or cubic behaviors, having a Poisson's ratio arbitrarily close to -1. Referring to the work by Sigmund (1994), Slann et al. (2015) conducted a numerical and experimental analysis on plates with centrosymmetric rectangular perforations and Mizzi et al. (2015) presented new auxetic metamaterials created with different slit patterns. Other models are described in recent reviews (Greaves et al. (2011); Milton (2015); Prawoto (2012); Zhou et al. (2013)).

In comparison with traditional materials, auxetic systems have some superior characteristics that can be exploited technologically, like higher resistance to indentation, larger fracture toughness and enhanced vibration absorption properties (Grima and Gatt (2010)). Relevant applications where auxetic systems may be particularly useful are the replacement of blood vessels (Evans and Alderson (2000)), the fabrication of smart filters and fasteners (Lakes (1987)), the design of structures with double curvature for

aircraft wings and car doors (Evans and Alderson (2000); Alderson and Alderson (2007)) and the production of auxetic fibers that are more resistant to pull-out (Evans and Alderson (2000)).

Here we present a porous auxetic structure, represented by a perforated sheet. The microstructured medium is shown in Fig. 1 in its undeformed configuration (a) and when it is stretched (b) and compressed (c): the negative value of the Poisson's ratio on the deformation of the medium is clear, and it is generated by relative rotation of internal parts of the microstructured medium causing an increase of porosity. A comparable design has been very recently proposed by Shan et al. (2015), who have simultaneously worked on a similar model. The novelty of the model in Fig. 1 with respect to other auxetic porous structures lies in its plane-isotropic behavior, ensuing from the threefold symmetry of the voids arrangement. In the present work, we consider for the first time a new class of porous materials with different relative inclinations and relative dimensions of the pores. The geometry of the single pores is carefully designed in order to reduce stress concentration. The study is focused on the modeling of the effect of the microstructural parameters on the effective properties considering both Poisson's ratio and Young's modulus, and it is based on an advanced comparison between numerical and experimental results both on effective properties and local fields.

We envisage that this structured medium can be of great value to devise novel stents and artificial blood vessels in biomedical engineering (Evans and Alderson (2000)) and to design the structural components of gas turbines constituted of perforated surfaces (Taylor et al. (2014)).

2. The isotropic auxetic porous medium

We consider a two-dimensional sheet containing holes, which are arranged in a hexagonal pattern as shown in Fig. 2a. The holes are inclined by an angle θ with respect to the normals to the hexagon sides, which have length l. As sketched in Fig. 2b, each hole consists of a rectangle of length a with two semicircles of radius b at the ends, introduced in order to reduce stress concentration.

We stress the fact that the proposed design makes the medium isotropic in the linear regime, as ensued from the threefold symmetry of the voids arrangement. In the following, we present a numerical and experimental study of the effective properties of the porous structure. We detail the mechanical behavior of the specimens tested experimentally and we also perform the

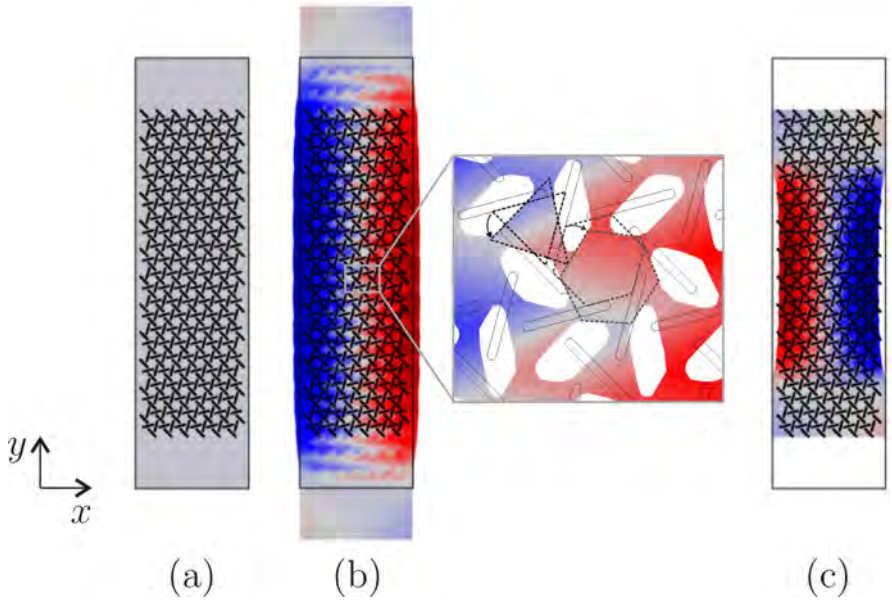

Figure 1: Auxetic porous medium proposed in this paper. (a) Undeformed configuration. (b) Deformed configuration under tensile forces. The inset shows a sketch of the deformation mechanism leading to negative Poisson's ratio; in particular, internal rotations of the bulk material are accommodated by enlargements of the pores, inducing a macroscopic volumetric expansion. (c) Deformed configuration under compressive forces. The red and blue colors indicate positive and negative horizontal displacements, respectively.

study of the unit cell in a periodic structure in order to obtain homogenised properties and to analyse the effect of the microstructural parameters.

The experimental tests have been performed at the Experimental Mechanics Laboratory of the Department of Mechanical, Chemical and Materials Engineering of the University of Cagliari. The constitutive properties of the solid phase were determined from standard uniaxial tensile tests on homogeneous specimens, engraved from the original Lexan polycarbonate sheet at different angles. The tests were performed on a Galdabini 5kN Quasar 5 testing machine under displacement control at a velocity rate of 2 mm/min. Lateral displacements were obtained with the supplementary use of a strain gauge. The behavior is isotropic and the Young's modulus, Poisson's ratio and yield stress were found to be equal to $E = 2.9$ GPa, $\nu = 0.35$ and $\sigma_y = 40$ MPa, respectively.

2.1. Analysis of the specimens of finite dimensions

First, we analyzed the finite structure in Fig. 1, which has a length of 420 mm, a heigth of 110 mm and a thickness of 3 mm. We built the model in the finite element package *Comsol Multiphysics* with three different configurations of the perforations. We reproduced the same models with real specimens, which are displayed in Fig. 3. These specimens are indicated by A, B and C in Fig. 3 and in the rest of the paper. The geometry of the perforations is identified by the following microstructural parameters: $a = 10$ mm, $b = 1$ mm, $l \approx 9$ mm and $\theta = 45°$. Samples B and C differ from sample A since the voids arrangement in B and C is rotated by 45° and 90°, respectively, relatively to A. This allows to test the system along three different directions if, for all samples, the uniaxial load is applied along the y direction.

The mesh of the finite element model, which was optimised with regards to convergence of results, consists of 95690 triangular elements and is refined in proximity of the holes.

The experimental specimens were produced using a 5-axis numerical controlled milling machine (DMU 60 p Hi Dyn). Cutting speed for the generation of the pores was adjusted to prevent residual stresses. Before the production of the specimens, we performed a series of photo-elastic experiments starting from a bench of stress-relaxed plates, in which a single hole was created using different cutting parameters. The optimal parameters were used to realize the specimens and an *a posteriori* test was performed to verify that residual

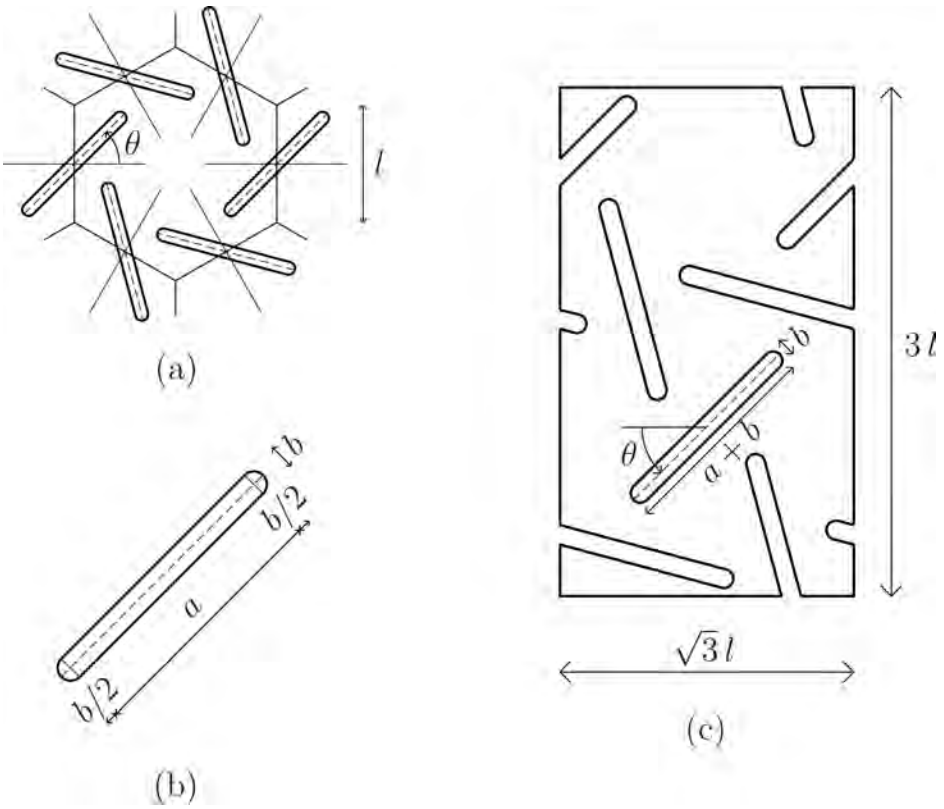

Figure 2: (a) Disposition of the perforations inside the two-dimensional structure, where l is the side of the hexagon and θ is the orientation angle of the perforations with respect to the normals to the hexagonal sides; (b) detail of each perforation, made of an elongated rectangle ending with two semicircles; (c) elementary cell representative of the infinite periodic structure.

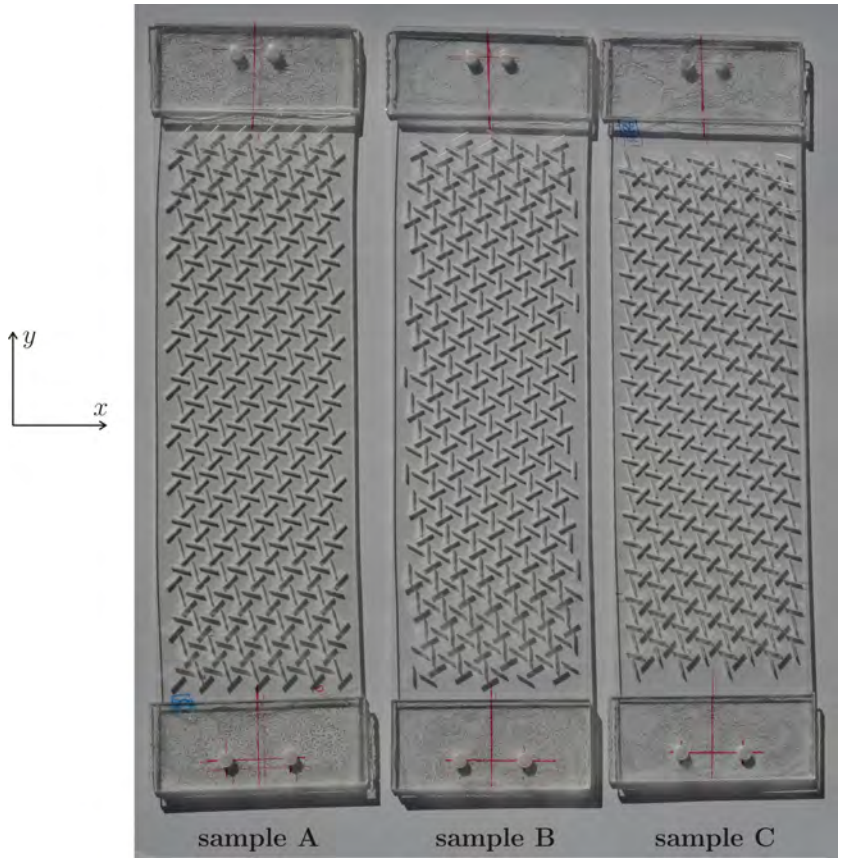

Figure 3: Specimens used in the experimental tests, where $a = 10$ mm, $b = 1$ mm, $l \approx 9$ mm and $\theta = 45°$ (refer to Fig. 2 for the definitions of the geometrical quantities). The disposition of the holes in samples B and C is rotated by 45° and 90°, respectively, with respect to the disposition in sample A.

stresses were below a minimum threshold in the final product. In particular, the cutting speed was about 950 mm/s for a cut depth of 0.1 mm.

We applied a uniform vertical traction at the top boundary and imposed zero vertical displacements at the bottom boundary. We considered a rectangular area in the central part of the model of dimensions 81 mm × 93 mm, which contains a sufficient amount of elementary cells and where the boundary layer effects are smaller. By referring to this area, we computed the average values of the normal stresses σ_{xx} and σ_{yy} and of the axial strains ε_{xx} and ε_{yy}. We solved the problem by performing a plane stress analysis, which is justified by the loading conditions and the small thickness. Simple

calculations lead to the following expressions for the Poisson's coefficient ν and the Young's modulus E:

$$\nu = \nu_{xy} = \frac{\varepsilon_{xx}\sigma_{yy} - \varepsilon_{yy}\sigma_{xx}}{\varepsilon_{xx}\sigma_{xx} - \varepsilon_{yy}\sigma_{yy}}, \quad E = E_x = E_y = \frac{\sigma_{xx}^2 - \sigma_{yy}^2}{\varepsilon_{xx}\sigma_{xx} - \varepsilon_{yy}\sigma_{yy}}. \qquad (1)$$

We report the results in the first column of Table 1, together with the outcomes obtained from the periodic study (discussed in Section 2.2) and from the experiments (described in Section 3.1).

	numerical (finite)	numerical (periodic)	experimental	
sample A	−0.552	−0.553	−0.551	ν
	248.8	254.8	—	E [MPa]
sample B	−0.552	−0.553	−0.550	ν
	247.8	254.8	—	E [MPa]
sample C	−0.557	−0.553	−0.548	ν
	247.0	254.8	—	E [MPa]

Table 1: Values of Poisson's ratio ν and Young's modulus E determined from the numerical computations on the finite and periodic models and from the experiments.

We also note that the maximum stress localization, computed as the ratio between the maximum von Mises stress, detected in proximity of the pores, and the average von Mises stress in the rectangular area, is equal to 21.7. This value is in a very good agreement with the stress concentration factor for a plate with an elliptical hole (see, for example, Anderson (2005), Chapter 2.2): when the major axis is equal to $a + b$ and a minor axis is equal to b, the stress concentration is equal to $1 + 2(a + b)/b = 23$. Such a result also indicates that the elastic interaction between pores does not induce an increase of stress localization.

2.2. Periodic system

Here we consider a perfectly periodic system made of repetitive cells, as that shown in Fig. 2c. We constructed a finite element model of the unit cell in *Comsol Multiphysics* by using a discretization of 10921 triangular elements. We imposed periodic conditions at the boundaries of the cell.

We applied firstly a macroscopic axial strain $\varepsilon_{xx} = 10^{-4}$, secondly a macroscopic axial strain $\varepsilon_{yy} = 10^{-4}$ and finally a macroscopic shear strain

$\varepsilon_{xy} = 10^{-4}$. For all three cases, we computed the average values of the relevant components of the stress tensors. We determined the Poisson's coefficient and the Young's modulus from Eqs. (1), while the shear modulus is given by

$$\mu = \mu_{xy} = \frac{\sigma_{xy}}{2\varepsilon_{xy}}. \tag{2}$$

The first and second cases ($\varepsilon_{xx} = 10^{-4}$ and $\varepsilon_{yy} = 10^{-4}$) yield the same results: $\nu = -0.553$ and $E = 2.548 \cdot 10^8$ Pa. From the third case ($\varepsilon_{xy} = 10^{-4}$) we obtained $\mu = 2.849 \cdot 10^8$ Pa, which is equal to the corresponding isotropic value $E/[2(1+\nu)]$. Returning back to the results in Table 1 we observe that the numerical findings confirm that the medium is auxetic and isotropic in the plane. The small discrepancies in the results for the finite samples considered in Section 2.1 are due to the boundary effects.

We recall that, for a generic cubic material, the Poisson's ratio depends on the stretching direction. Denoting by β the angle between the stretching direction and the principal x axis of the structure, the Poisson's ratio can be calculated by using the following formula (see, for example, Cabras and Brun (2014)):

$$\nu(\beta) = -\frac{\cos^2\beta \sin^2\beta \left(2/E - 1/\mu\right) - \left(\sin^4\beta + \cos^4\beta\right)\nu/E}{\left(\sin^4\beta + \cos^4\beta\right)/E + 1/\mu - 2\nu/E}, \tag{3}$$

where E and ν are determined from a tensile test and μ from a shear test with $\beta = 0, \pi/2$. In Fig. 4 we show the polar diagrams of $\nu(\beta)$ for the structured medium proposed in this paper and for a generic cubic material. It is clear that the present model is isotropic in the plane, since ν does not vary with β. On the other hand, the Poisson's ratio of a generic cubic material depends on β, and it can even be negative in some directions but positive in others. Obviously, the variation of ν with the direction of the applied load can have significant drawbacks in practical applications.

2.2.1. Effect of microstructural parameters

We investigated how the length ratios a/l and b/l and the orientation angle of the voids θ influence the constitutive properties of the perforated sheet. In Fig. 5 we show how the Poisson's ratio and the Young's modulus vary with the ratio a/l for different values of θ and for $b/l = 1/9$ (a) and for $b/l = 1/18$ (b). The results obtained for the particular values of the parameters characterizing the specimens in Fig. 3 are highlighted by black dots in Fig. 5a.

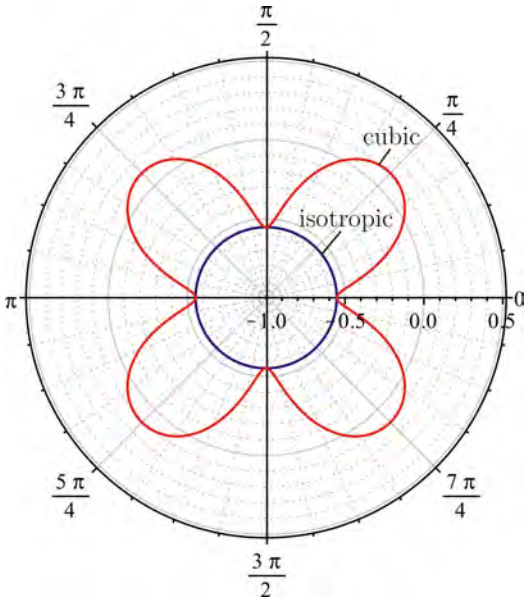

Figure 4: Polar diagrams of the Poisson's ratio as a function of the angle β, defining the orientation of the stretching direction with respect to a principal axis of the structure, for the model described in this paper (blue color) and for a generic cubic material with $\mu \neq E/[2(1+\nu)]$ (red color).

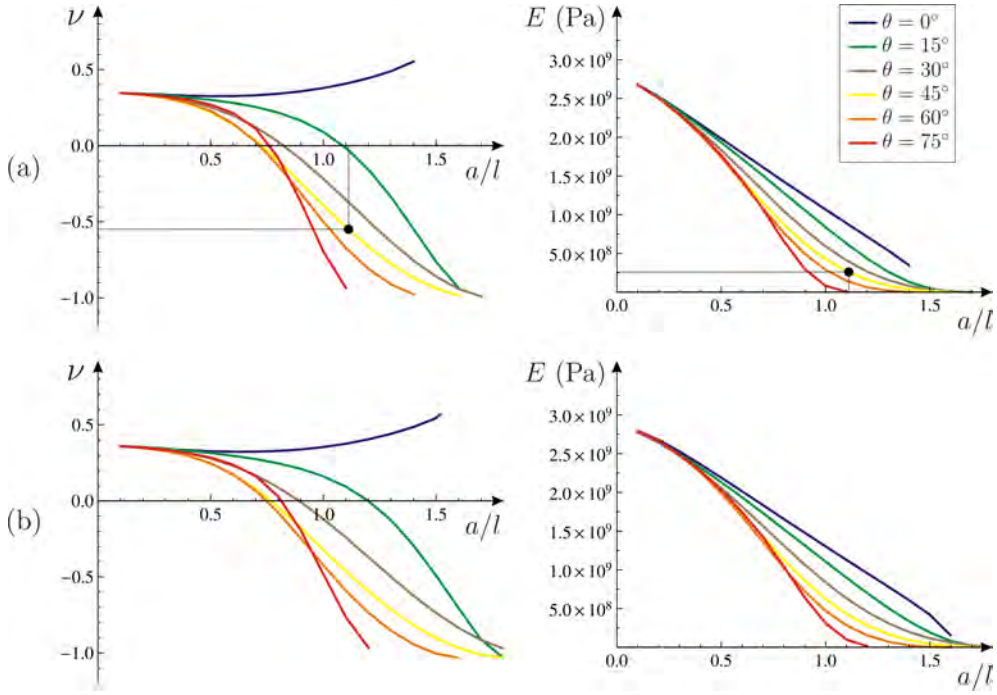

Figure 5: Poisson's ratio ν and Young's modulus E as functions of a/l for different values of θ and for $b/l = 1/9$ (a) and $b/l = 1/18$ (b). The dots in part (a) indicate the values of ν and E for the samples in Fig. 3 (see also Table 1).

For the sake of completeness we point out that, in order to avoid the merging of the holes, their length a must be kept below a limit, which depends on the angle θ. This limit is obtained from geometrical considerations and is equal to

$$a_1 = \frac{\sqrt{3} + 2\sin(2\theta)}{\cos\theta + \sqrt{3}\sin\theta} l - \frac{4\sqrt{3}}{3} b \quad \text{for } \theta < \theta^*,$$
$$a_2 = l\sin\theta - \sqrt{\frac{4b^2}{3} - l^2\cos^2\theta} \quad \text{for } \theta > \theta^*. \tag{4}$$

The transition value

$$\theta^* \approx \frac{\pi}{2} - \frac{2(3-\sqrt{3})}{3}\frac{b}{l} \tag{5}$$

is calculated by solving the equation $a_1(\theta) = a_2(\theta)$. We also note that Eq. (4b) requires that $|\cos(\theta)| < 2b/(\sqrt{3}l)$.

Fig. 5 shows that for low values of a/l, namely for short voids, the Poisson's coefficient of the perforated sheet is close to the value of the intact material, equal to 0.35 in this case. As the relative length of the holes a/l is increased, the value of ν diminishes and it reaches a transition value beyond which the structured medium becomes auxetic ($\nu < 0$). We also note that it is possible to set the geometrical parameters in order to have a Poisson's coefficient close to the limit -1. At the same time, the elastic modulus obviously decreases at increasing a/l, hence the material becomes softer.

It is interesting to note - and not trivial - that, generally, ν and E can be decreased by increasing the orientation angle of the voids θ, for a fixed value of the ratio a/l. The comparison between the insets (a) and (b) reveals that, for specified values of the geometrical parameters a/l and θ, the coefficients ν and E can be decreased by making the perforations wider.

3. Experimental validation

We tested in the laboratory the three specimens indicated with A, B and C in Fig. 3. In order to perform a comparative analysis with numerical simulations, we made use of an advanced Digital Image Correlation technique and photoelasticity.

3.1. Digital Image Correlation

We obtained the displacement and strain fields within the samples by means of the Digital Image Correlation (DIC) technique. Digital Image Cor-

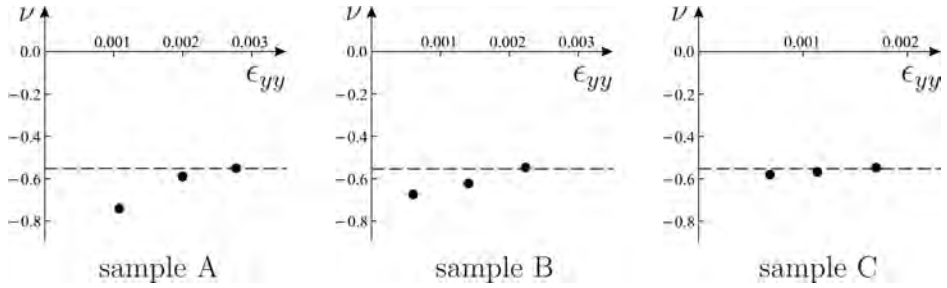

Figure 6: Experimental values of the Poisson's ratio for the samples A, B and C in Fig. 3, obtained for different values of the axial strain ε_{yy}. The horizontal dashed line $\nu = -0.533$ represents the theoretical value of the Poisson's coefficient for the infinite periodic structure (see second column of Table 1).

relation is a non-interferometric experimental technique able to estimate bi-dimensional (tri-dimensional in its stereo version) displacement fields. Its basic assumption is the constancy of the intensity of each point during motion. Thus, if the surface texture is not uniform, it is possible to correlate each point in the reference image with the corresponding point in the deformed image. Formally, this results in the well-known optical flow equation

$$\frac{\partial I}{\partial x}\dot{u} + \frac{dI}{dy}\dot{v} + \frac{dI}{dt} = 0, \tag{6}$$

where u and v are the x and y displacement components and I is the image intensity. Looking at this equation it is apparent that it involves two unknowns, i.e. the velocity components $\dot{u}$ and $\dot{v}$, hence an auxiliary condition has to be specified. The most commonly used solution to this problem is the Lucas-Kanade approach (Lucas and Kanade (1981)), which assumes that the displacement field can be locally approximated by a simple function, which is usually an affine transform. Provided that a sufficiently large number of pixels is involved in the least square fit, the set of parameters controlling the mapping can be identified by reverse calibration (usually by a Newton-like iterative algorithm); moreover, by sampling the images at different locations, full-field data can be obtained by interpolating the displacements at the sampling points.

From the practical viewpoint, performing the measurements requires the comparison of two images acquired before and after each load increment. To comply with the basic hypothesis of the technique, i.e. pixel intensity does not change with motion, the illumination has to be (nearly) isotropic, the

specimen surface needs to be opaque (to minimize directional components associated with reflection) and the surface has to be textured with a chaotic pattern (to ensure its uniqueness) (see Del Bimbo et al. (1995)).

The tests on the porous specimens were performed under displacement control. We applied a series of 5 displacement steps (0.5 mm each) along the y direction on the photoelastic bench and the experimental results were taken under static conditions. The applied displacement was such that the local stress did not exceed the yield limit on the basis of Finite Element simulations. The absence of yielding was verified by an *a posteriori* photoelastic inspection in the vicinity of the pores groove tips, where no significant residual stress was detected after unloading the specimens. Images were acquired using a D700 Nikon camera with a 200 mm focal lens to reduce prospective artifacts. To remove the influence of the Bayer pattern, the resulting (raw) images were binned using a 2×2 mask. Then they were processed using an in-house-developed software (ofTri). Finally, the output data (i.e. nodal displacements and strains) were post-processed to compute the Poisson's ratio. The standard deviation of displacements, when acquired using the standard Digital Image Correlation, is relatively large: indeed, due to the statistical approach, it depends on the square root of the number of pixels involved in the local computation. Moreover, each sampling is uncorrelated, thus the strain uncertainty is about 250 μm/m. To reduce this value, we replaced the local measurement with a global approach: instead of using a local model of the displacement field, we opted for a global description using a finite-element-like approach (Sun et al. (2005)). Displacements inside each element are controlled by nodal parameters, which make the model global being shared with adjacent elements. In this way the standard deviation of displacements is significantly reduced (Hild and Roux (2012)) and the solution is more robust.

For each sample, we considered a rectangular region in the central part of the specimen, where the boundary layer effects are smaller. We calculated the averages of the horizontal displacements u in the left (L) and right (R) sides of the rectangle and the averages of the vertical displacements v in the bottom (B) and top (T) boundaries. Accordingly, the experimental value of the Poisson's ratio was estimated as

$$\nu^{exp} \approx -\frac{\langle \varepsilon_{xx} \rangle}{\langle \varepsilon_{yy} \rangle} = -\frac{\left(\langle u^R \rangle - \langle u^L \rangle \right) / L_x}{\left(\langle v^T \rangle - \langle v^B \rangle \right) / L_y}, \tag{7}$$

where $\langle q \rangle$ represents the average value of the quantity q, L_x and L_y are

the dimensions of the horizontal and vertical sides of the rectangle, while ε_{xx} and ε_{yy} stand for the axial strains in the x and y directions. We also considered different values of the applied load, yielding different strains ε_{yy}, but restricting the range of deformation within the linear regime.

We report the results for the three specimens A, B and C and for three values of the applied load in Fig. 6. The experimental values of ν^{exp} are indicated by black dots. We note that, as ε_{yy} increases, the data tend to converge to the horizontal dashed line, which indicates the theoretical value determined from the periodic analysis described in Section 2.2. Thus, the load needs to be sufficiently large to allow for the necessary adjustment of the specimen. Fig. 6 shows that the proposed structured medium is auxetic, since the Poisson's ratio is negative. In addition, the latter does not depend significantly on the loading direction, hence the material is isotropic in the plane.

The experimental values of the Poisson's ratio for the three specimens are given in the third column of Table 1, where we report the values at the highest deformation ε_{yy}. The comparison of the test outcomes with the values in the first and second columns, obtained from the numerical analysis on the finite and periodic model respectively, reveals a very good agreement between the numerical and experimental data.

In Fig. 7 we plot the contour maps of the horizontal (a) and vertical (b) displacements of the sample A, obtained both experimentally (left) and numerically (right). The internal black regions represent the perforations, for which the displacement field could not be evaluated. It is apparent that the correspondence between the two studies is excellent. The horizontal displacement field confirms that the behavior of the medium is auxetic.

The same comparative analysis is reported in Figs. 8 and 9 for the samples B and C, respectively. Again the agreement is excellent and the auxetic behavior is evident.

3.2. Photoelasticity

We used photoelasticity to evaluate the stress distribution in the porous medium. In Fig. 10a we show the difference between the principal stresses, namely $\sigma_1 - \sigma_2$, obtained experimentally with a circular polariscope. The structure exhibits stress concentration in proximity of the ends of the perforations, as expected. Fig. 10b presents the $\sigma_1 - \sigma_2$ distribution derived from the finite element model. The comparison between the experimental and numerical outcomes is remarkable.

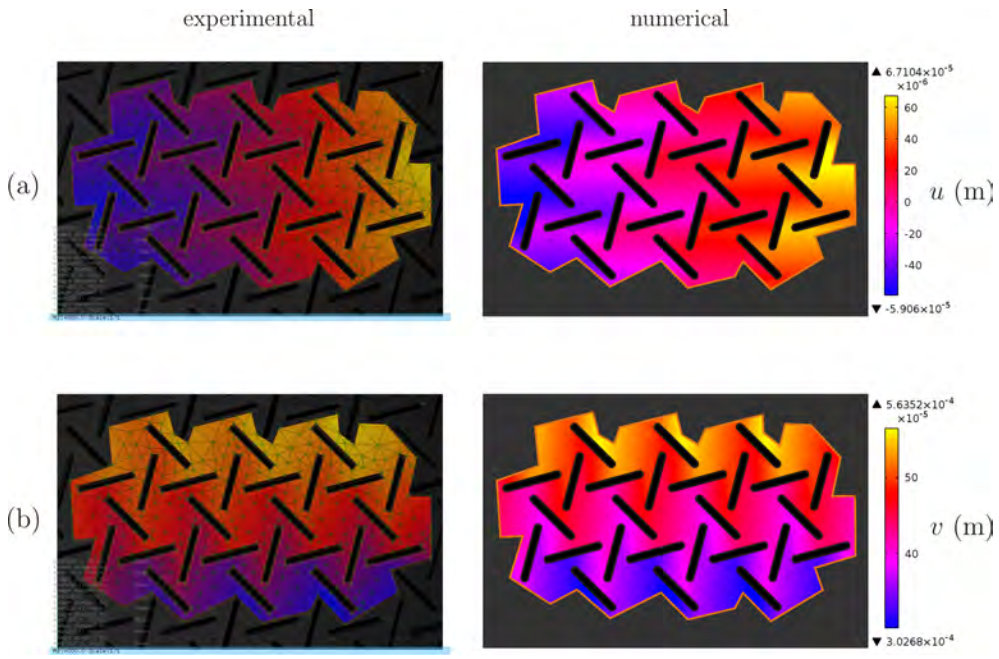

Figure 7: Contour maps of the horizontal (a) and vertical (b) components of the displacement field, obtained from the lab tests and from the finite element simulations, for the sample A displayed in Fig. 3. The average axial strain is $\varepsilon_{yy} = 2.77 \cdot 10^{-3}$.

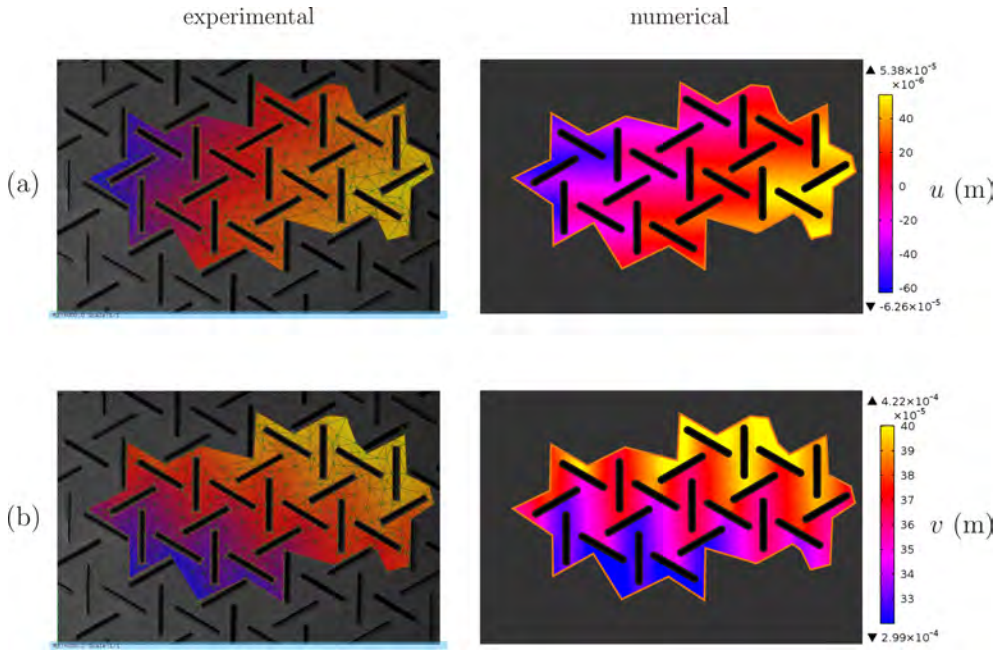

Figure 8: Contour maps of the horizontal (a) and vertical (b) components of the displacement field, obtained from the lab tests and from the finite element simulations, for the sample B shown in Fig. 3. The macroscopic axial strain is $\varepsilon_{yy} = 2.24 \cdot 10^{-3}$.

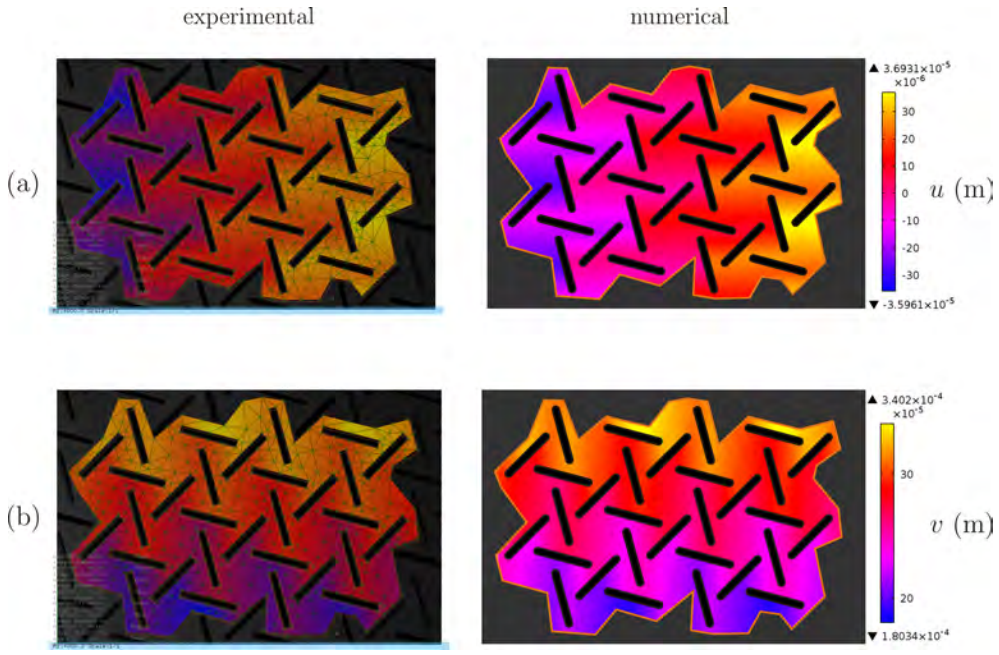

Figure 9: Contour maps of the horizontal (a) and vertical (b) components of the displacement field, obtained from the lab tests and from the finite element simulations, for the sample C shown in Fig. 3. The macroscopic average axial strain is $\varepsilon_{yy} = 1.70 \cdot 10^{-3}$.

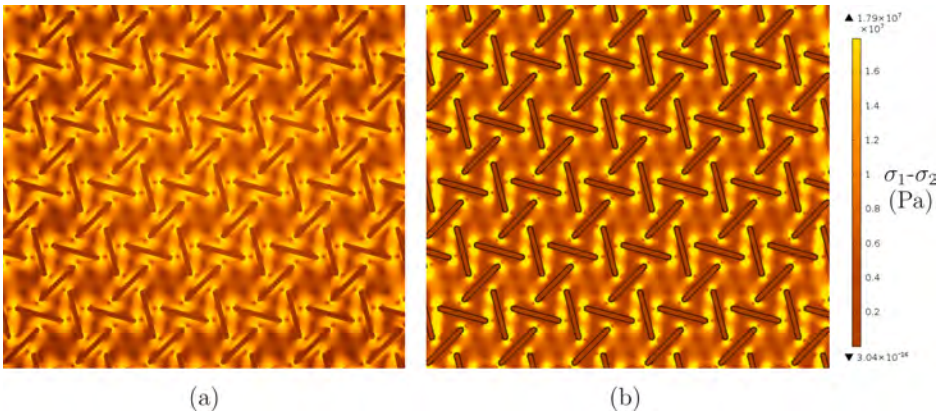

Figure 10: Contour maps of the difference in the first and second principal stresses $\sigma_1 - \sigma_2$ obtained experimentally with a circular polariscope (a) and numerically by means of finite element computations (b).

4. Conclusions

We have proposed the design of a two-dimensional porous solid, which exhibits a negative Poisson's ratio. The arrangement of the microstructure makes the effective behavior isotropic. The planar auxetic and isotropic behavior of the considered porous medium has been observed experimentally on three specimens, characterized by a 45° rotation of the pores disposition relative to each other and loaded in the same direction. The experimental findings have been corroborated by numerical computations on finite models, reproducing the real specimens. The numerical study of the unit cell has given a more refined evaluation of the effective properties, independent of boundary conditions. It has confirmed the perfect isotropy of the porous material, so that negative Poisson's ratio is omni-directional and independent on the direction of the applied load. The parametric study of the dependance of the effective properties on the geometrical microstructural parameters of the system shows, in particular, that the Poisson's ratio is strongly influenced by the relative orientation of the pores. Both advanced Digital Image Correlation technique and photoelasticity confirm the auxetic behavior and the isotropy, and they have been found to be in excellent agreement with numerical simulations.

We believe that this structure, which is simple to manufacture and easily adaptable to specific requirements, may be exploited in a great variety of industrial applications, considering also that the effective behavior of the porous material is scale-independent.

Acknowledgments

G.C. and M.B. acknowledge the financial support of Regione Autonoma della Sardegna (LR7 2010, grant 'M4' CRP-27585). The authors wish to thank Mr. Gianluca Marongiu for the preparation of the specimens, and Prof. Francesco Aymerich and Dr. Agostino Cerioni for the help in testing the material properties of the intact structure.

References

Alderson, A., Alderson, K.L., 2007. Auxetic Materials. Proc. Inst. Mech. Eng., Part G, J. Aero. Eng. 221, 565-575. (doi:10.1243/09544100JAERO185)

Anderson, T.L., 2005. Fracture Mechanics. Fundamentals and Applications, 3rd ed. Taylor & Francis, Boca Raton.

Baughman, R.H., Shacklette, J.M., Zakhidev, A.A., Stafström, S., 1998. Negative Poisson's ratio as a common feature of cubic metals. Nature 392, 362-365. (doi:10.1038/32842)

Bertoldi, K., Reis, P.M., Willshaw, S., Mullin, T., 2010. Negative Poisson's Ratio Behavior Induced by an Elastic Instability. Adv. Mater. 22(3), 361-366. (doi:10.1002/adma.200901956)

Cabras, L., Brun, M., 2014. Auxetic two-dimensional lattices with Poisson's ratio arbitrarily close to -1. Proc. R. Soc. Lond. A 470, 20140538. (doi: 10.1098/rspa.2014.0538)

Chen, Y.J., Scarpa, F., Farrow, I.R., Liu, Y.J., Leng, J.S., 2013. Composite flexible skin with large negative Poisson's ratio range: numerical and experimental analysis. Smart Mater. Struct. 22, 045005. (doi:10.1088/0964-1726/22/4/045005)

Chen, Y.J., Scarpa, F., Remillat, C., Farrow, I.R., Liu, Y.J., Leng, J.S., 2014. Curved Kirigami SILICOMB cellular structures with zero Poissons ratio for large deformations and morphing. J. Intell. Mater. Syst. Struct. 25(6), 731-743. (doi:10.1177/1045389X13502852)

Choi, J.B., Lakes, R.S., 1995. Analysis of elastic modulus of conventional foams and of re-entrant foam materials with a negative Poisson's ratio. Int. J. Mech. Sci. 37(1), 51-59. (doi:10.1016/0020-7403(94)00047-N)

Del Bimbo, A., Nesi, P., Sanz, J., 1995. Analysis of optical flow constraints. IEEE Trans. Image Process. 4(4), 460-469. (doi:10.1109/83.370674)

Evans, K.E., 1991. Auxetic polymers: a new range of materials. Endeavour 15(4), 170-174. (doi:10.1016/0160-9327(91)90123-S)

Evans, K.E., Alderson, K.L., 2000. Auxetic materials: the positive side of being negative. Eng. Sci. Educ. J. 9(4), 148-154.

Greaves, G.N., Greer, A.L., Lakes, R.S., Rouxel, T., 2011. Poisson's ratio and modern materials. Nat. Mater. 10, 823-827. (doi:10.1038/nmat3134)

Grima, J.N., Alderson, A., Evans, K.E., 2005. Auxetic behaviour from rotating rigid units. Phys. Status Solidi B 242(3), 561-575. (doi:10.1002/pssb.200460376)

Grima, J.N., Gatt, R., 2010. Perforated Sheets Exhibiting Negative Poisson's Ratios. Adv. Eng. Mater. 12(6), 460-464. (doi:10.1002/adem.201000005)

Grima, J.N., Gatt, R., Farrugia, P.S., 2008. On the properties of auxetic meta-tetrachiral structures. Phys. Status Solidi B 245(3), 511-520. (doi:10.1002/pssb.200777704)

Grima, J.N., Gatt, R., Zammit, V., Williams, J.J., Evans, K.E., Alderson, A., Walton, R.I., 2007. Natrolite: A zeolite with negative Poisson's ratios. J. Appl. Phys. 101, 086102. (doi:10.1063/1.2718879)

Grima, J.N., Jackson, R., Alderson, A., Evans, K. E., 2000. Do Zeolites Have Negative Poisson's Ratios? Adv. Mater. 12, 1912-1918. (doi:10.1002/1521-4095(200012)12:24<1912::AID-ADMA1912>3.0.CO;2-7)

Hild, F., Roux, S., 2012. Comparison of local and global approaches to digital image correlation. Exp. Mech. 52, 1503-1519. (doi:10.1007/s11340-012-9603-7)

Lakes, R.S., 1987. Foam structures with a negative Poisson's ratio. Science 235, 1038-1040. (doi:10.1126/science.235.4792.1038)

Love, A.E.H., 1944. A treatise on the mathematical theory of elasticity, 4th ed. Dover Publications, New York.

Lucas, B.D., Kanade, T., 1981. An iterative image registration technique with an application to stereo vision. Proc. of Imaging Understanding Workshop 130, 121-130.

Milton, G.W., 2015. New examples of three-dimensional dilational materials. Phys. Status Solidi B 252(7), 1426-1430. (doi:10.1002/pssb.201552297)

Mizzi, L., Azzopardi, K.M., Attard, D., Grima, J.N., Gatt, R., 2015. Auxetic metamaterials exhibiting giant negative Poisson's ratio. Phys. Status Solidi RRL 9(7), 425-430. (doi: 10.1002/pssr.201510178)

Norris, A.N., 2006. Poisson's ratio in cubic materials. Proc. R. Soc. Lond. A 462(275), 3385-3405. (doi:10.1098/rspa.2006.1726)

Prall, D., Lakes, R.S., 1997. Properties of a chiral honeycomb with a poisson's ratio of -1. Int. J. Mech. Sci. 39(3), 305-314. (doi:10.1016/S0020-7403(96)00025-2)

Prawoto, Y., 2012. Seeing auxetic materials from the mechanics point of view: A structural review on the negative Poissons ratio. Comput. Mater. Sci. 58, 140-153. (doi:10.1016/j.commatsci.2012.02.012)

Scarpa, F., Tomlin, P.J., 2000. On the transverse shear modulus of negative Poisson's ratio honeycomb structures. Fatigue Fract. Eng. M. 23, 717-720. (doi:10.1046/j.1460-2695.2000.00278.x)

Shan, S., Kang, S.H., Zhao, Z., Fang, L., Bertoldi, K., 2015. Design of planar isotropic negative Poissons ratio structures. Extreme Mechanics Letters 4, 96-102. (doi:10.1016/j.eml.2015.05.002)

Shen, J., Zhou, S., Huang, X., Xie, Y.M., 2014. Simple cubic three-dimensional auxetic metamaterials. Phys. Status Solidi B 251(8), 1515-1522. (doi:10.1002/pssb.201451304)

Sigmund, O., 1994. Materials with prescribed constitutive parameters: an inverse homogenization problem. Int. J. Solids Structures 31(17), 2313-2329. (doi: 10.1016/0020-7683(94)90154-6)

Slann, A., White, W., Scarpa, F., Boba, K., Farrow, I., 2015. Cellular plates with auxetic rectangular perforations. Phys. Status Solidi B 252(7), 1533-1539. (doi: 10.1002/pssb.201451740)

Song, F., Zhou, J., Xu, X., Xu, Y., Bai, Y., 2008. Effect of a Negative Poisson Ratio in the Tension of Ceramics. Phys. Rev. Lett. 100, 245502. (doi:10.1103/PhysRevLett.100.245502)

Spadoni, A., Ruzzene, M., 2012. Elasto-static micropolar behavior of a chiral auxetic lattice. J. Mech. Phys. Solids 60(1), 156-171. (doi:10.1016/j.jmps.2011.09.012)

Sun, Y., Pang, J., Wong, C., Su, F., 2005. Finite element formulation for a digital image correlation method. Appl. Opt. 44(34), 7357-7363. (doi:10.1364/AO.44.007357)

Taylor, M., Francesconi, L., Gerends, M., Shanian, A., Carson, C., Bertoldi, K., 2014. Low Porosity Metallic Periodic Structures with Negative Poisson's Ratio. Adv. Mater. 26(15), 2365-2370. (doi:10.1002/adma.201304464)

Timoshenko, S.P., 1955. Strength of Materials, Part 1, Elementary Theory and Problems, 3rd ed. Van Nostrand, New York.

Yeganeh-Haeri, A., Weidner, D.J., Parise, J.B., 1992. Elasticity of α-cristobalite: a silicon dioxide with a negative Poisson's ratio. Science 257, 650-652. (doi:10.1126/science.257.5070.650)

Zhou, M., Du, Z., Lu, G., 2013. Textile Materials and Structures with Negative Poisson's Ratio - An Overview. J. Fiber Bioeng. Inf. 6(4), 349-367. (doi:10.3993/jfbi12201302)